Journal of Physics: Condensed Matter

PAPER

Torsion-induced vortex switching and skyrmion-like state in ferroelectric nanodisks

To cite this article: Shuai Yuan *et al* 2018 *J. Phys.: Condens. Matter* **30** 465304

IOP Publishing
Journal of Physics: Condensed Matter
J. Phys.: Condens. Matter **30** (2018) 465304 (15pp)
https://doi.org/10.1088/1361-648X/aae5e9

Torsion-induced vortex switching and skyrmion-like state in ferroelectric nanodisks

Shuai Yuan[1,2,3], Weijin Chen[2,3], Jianyi Liu[2,3], Yulan Liu[1], Biao Wang[2] and Yue Zheng[2,3]

[1] School of Engineering, Sun Yat-sen University, Guangzhou 510275, People's Republic of China
[2] State Key Laboratory of Optoelectronic Materials and Technologies, School of Physics, Sun Yat-sen University, Guangzhou 510275, People's Republic of China
[3] Micro & Nano Physics and Mechanics Research Laboratory, School of Physics, Sun Yat-sen University, Guangzhou 510275, People's Republic of China

E-mail: zhengy35@mail.sysu.edu.cn, wangbiao@mail.sysu.edu.cn and stslyl@mail.sysu.edu.cn

Received 23 August 2018, revised 24 September 2018
Accepted for publication 3 October 2018
Published 30 October 2018

Abstract

The controllability of vortex state in ferroelectric nanodisks under the effect of external torsion is investigated in this work based on phase-field simulation. We discover a novel Bloch skyrmion-like state in ferroelectric nanodisks due to the combining effect of the torsion and the depolarization field. Moreover, a new strategy is proposed to achieve deterministic switching of the vortex chirality in the ferroelectric nanodisks. On the one hand, if a fixed external electric field is applied to the nanodisk, the vortex chirality can be switched by the torsion force. On the other hand, if we apply a fixed torsion force to the nanodisk, the vortex chirality can be readily switched by an external electric field. The feasibility of both mechanical and electrical switching of the vortex in the ferroelectric nanodisks is based on the trilinear coupling between the toroidization, polarization and shear strain of the system. The influences of temperature, electric field, torsion, and size of the nanodisk on the control of the vortex state are further revealed. Our findings shed light on the practical control and application of ferroelectric dipole vortices.

Keywords: ferroelectrics, vortex, torsion, chirality switching, skyrmion

(Some figures may appear in colour only in the online journal)

1. Introduction

In recent years, ferroelectric materials have attracted intensive attention from researchers due to their excellent electrical, optical, mechanical and multi-field coupling properties. By utilizing these properties, it is promising to fabricate advanced functional electronic and mechatronic devices based on ferroelectric materials. As we know, the polarization vector is often ordered rectilinearly in different regions of ferroelectric bulk materials. The regions with the same rectilinear polarization vectors are called domains, in which the orientation and magnitude of polarization are uniform. However, as the ferroelectric size is reduced to nanoscale, the rectilinear polarization distribution is unstable under open-circuited boundary conditions. A new toroidal order of the electric dipoles in low-dimensional ferroelectric nanostructures, termed vortex state, forms due to the strong depolarization field and size effect. Vortex state can be regarded as a kind of topological defects with a toroidal and closure distribution of the magnetic spins or electric dipoles existing in ferroic materials. In fact, vortex state was well known and first predicted by Landau and Lifshitz in 1930s [1] and by Kittel in 1940s [2], showing that formation of circular domains was likely in ferromagnetic nanodots owing to the surface boundary conditions. About seventy years later, vortex state was demonstrated by Naumov *et al* in ferroelectric nanostructures based on the first-principle-derived approach in 2004 [3]. After that, it was explored in experiments via the use of piezoresponse force microscopy

(PFM) and aberration-corrected transmission electron microscopy (TEM) [4–10]. More recently, ferroelectric vortex states were also observed experimentally in ferroelectric-dielectric superlattices, and their characteristics were consistent with simulations based on phase-field methods [11–15].

Ferroelectric vortex states have attracted considerable attention due to the potential applications in next-generation ferroelectric memories for its small size as well as their novel properties compared with conventional ferroelectric domain structures [16–18]. A series of novel static and dynamic properties of ferroelectric vortex states have been revealed in previous works, including the appearance of various exotic states [9, 19], field-induced vortex-polar transformation [20–22], stress/strain-induced vortex–vortex transformation [23, 24], and the superior electromechanical response owing to vortex-polar coupling [25, 26], etc.

As far as applications are concerned, the possibility of controlling the chirality of dipole vortex reveals an exciting opportunity to develop new nanoscale memories and logic devices. The strong stability of vortex state in ferroelectrics makes it an attractive alternative to non-volatile memory; nevertheless, practical control is quite challenging because of the conjugate relations between dipole toroidal moment and the curl of **E** [27]. Although chirality control by a curled electric field has been proposed [21], many difficulties in practice to generate and apply an external curled electric stimulus in nanoscale is inevitable. In fact, the inhomogeneous electric field parallel to the vortex plane is considered to provide effective control of the intrinsic vortex chirality [20]. As an alternative, it has been investigated to control vortex chirality by a homogeneous electric field in an asymmetric ferroelectric nanodisk [28]. Recently, Chen *et al* has proposed that vortex switching can be facilitated by mechanical strain or stress [29], by breaking the symmetry of ferroelectric vortex via mechanical loads (e.g. the substrate clamping, dislocation as well as AFM tip loading). Consequently, even a system with high geometric symmetry can also achieve vortex switching by a homogeneous electric field. More recently, via the application of tensile and compressive stress in defective nanoplatelets, a mechanical strategy of vortex switching has also been proposed [30]. Despite the advances made thus far, discovery of alternative vortex switching strategies which are facile to implement is still necessary.

It is noteworthy that the contribution of shear stress to the electrostrictive effect in ferroelectrics has rarely been studied to date; however, it is effective for controlling the polarization reversal [31]. Here we propose a new switching mechanism to manipulate the chirality of dipole vortex in ferroelectric nanodisks via shear stress engineering. Due to the electromechanical coupling effect between shear stress and polarization components in ferroelectrics, torsion force should affect not only formation but also transformation of the vortex states. As shown in figure 1, under the effect of torsion, a novel Bloch-type skyrmion-like state in ferroelectric nanodisks can be induced. More importantly, via a combined manipulation of torsion and homogenous electric field, a deterministic chirality switching of dipole vortex is realized in this work. The influences of temperature, electric field, torsion, and cross-sectional diameter of the nanodisk on the vortex switching behaviors are also explored. Our results should be instructive for the control and applications of ferroelectric dipole vortices.

2. Models and methodology

2.1. Phase-field model

To characterize the vortex states in nanodisks under the stimulus of torsion and electric field, we perform phase-field simulations in this work. According to previous studies [32–35], we choose the spontaneous polarization field $\mathbf{P}(\mathbf{r}, t) = (P_1, P_2, P_3)$ as the order parameter to represent the dipole configuration. The Helmholtz free energy is selected to describe the total free energy in the system, which is composed of two parts including volume integral and surface integral, i.e.

$$F(\mathbf{P}, \nabla\mathbf{P}, \varepsilon, \mathbf{E}) = \int_V [f_{\mathrm{Land}}(\mathbf{P}) + f_{\mathrm{elas}}(\mathbf{P}, \varepsilon) + f_{\mathrm{grad}}(\nabla\mathbf{P}) + f_{\mathrm{elec}}(\mathbf{P}, \mathbf{E})]\, dV + \int_S f_{\mathrm{surf}}(\mathbf{P})\, \mathrm{d}S \tag{1}$$

where f_{Land}, f_{elas}, f_{grad}, f_{elec} and f_{surf} are the densities of the bulk Landau energy, the gradient energy, the elastic energy, the electrostatic energy and the surface energy, respectively. **E** is the electric field, ε denotes total strain tensor, and $\nabla\mathbf{P}$ represents the gradient of **P**. $\nabla\mathbf{P}$ and ε are second-order tensors. V and S denote the volume and surfaces of the system, respectively.

The bulk free energy density f_{Land} is expressed as a Taylor series expansion as a power of **P**. Here we adopt a sixth-order polynomial to characterize the Landau energy density of $\mathrm{PbTiO_3}$ (PTO) [36]:

$$f_{\mathrm{Land}} = a_1 \sum_i P_i^2 + a_{11} \sum_i P_i^4 + a_{12} \sum_{i>j} P_i^2 P_j^2 + a_{111} \sum_i P_i^6 + a_{112} \sum_{i>j} (P_i^4 P_j^2 + P_j^4 P_i^2) + a_{123} \prod_i P_i^2 \tag{2}$$

where a_i, a_{ij} and a_{ijk} are expansion coefficients, and the indexes i, j and k range from 1 to 3.

To simulate the spatial inhomogeneity of the polarization field, the gradient energy term f_{grad} is included into Helmholtz free energy of the system. Similarly, it is written as a Taylor series expansion as a power of $\nabla\mathbf{P}$. For the sake of simplicity, we express this term in its lowest order of expansion as follows:

$$f_{\mathrm{grad}} = \frac{1}{2} \nabla\mathbf{P} : \mathbf{g} : \nabla\mathbf{P} \tag{3}$$

where **g** represents the coefficient of gradient energy as a fourth-order tensor. It should be noted that there only exist three independent parameters here in **g**, i.e. g_{11}, g_{12}, g_{14} and g_{44}. The corresponding subscripts are based on Voigt notations [37].

The elastic energy is considered according to Khachaturyan's microscopic elastic theory [38]. The total strain is composed of elastic strain and stress-free strain and the elastic energy is only associated with the former. In

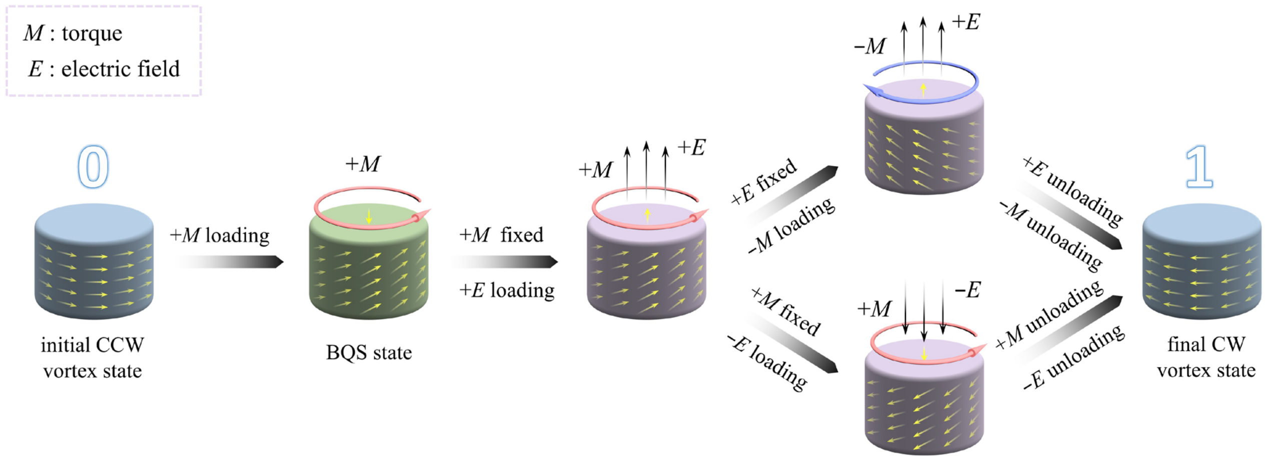

Figure 1. Schematic of torsion-induced Bloch-type quasi-skyrmion (BQS) state and the control of vortex chirality by Class-I switching and Class-II switching. M and E denote the torsion and electric field, respectively. The initial CCW and the final CW vortex states are defined as state '0' and '1', respectively. For Class-I switching, if we apply a fixed external electric field along z-axis to the nanodisk, the two vortex states '0' and '1' can be switched to each other by reversing the torsion force. For Class-II switching, if we apply a fixed torsion force to the nanodisk, the two vortex states '0' and '1' can be switched to each other by reversing the external electric field along z-axis.

ferroelectrics, eigenstrains related to the electrostrictive effect are stress-free, and make no contribution to elastic energy. In fact, the elastic strain and the corresponding producing stress together contribute to elastic free energy term. Thus, we describe f_{elas} in the form of tensor below:

$$f_{\text{elas}} = \frac{1}{2}\mathbf{e}:\mathbf{C}:\mathbf{e} = \frac{1}{2}\left(\varepsilon-\varepsilon^{0}\right):\mathbf{C}:\left(\varepsilon-\varepsilon^{0}\right) \tag{4}$$

where $\mathbf{C}$ is the elastic stiffness tensor, and $\mathbf{e}$ and ε^0 denote elastic strain tensor and eigenstrain tensor, respectively. In ferroelectrics, according to the electrostrictive effect, the eigenstrain ε^0 is expressed as $\varepsilon^0 = \mathbf{P}\cdot\mathbf{Q}\cdot\mathbf{P}$. Both $\mathbf{C}$ and $\mathbf{Q}$ are fourth-order tensors. Furthermore, with cubic paraelectric phase in a ferroelectric, only three nonzero components in $\mathbf{C}$ and $\mathbf{Q}$ exist, i.e. C_{11}, C_{12}, C_{44} and Q_{11}, Q_{12}, Q_{44}.

The electrostatic energy is included because the long-range interaction of dipoles in ferroelectrics is important. According to the continuum theory [33, 39], we express the electrostatic energy density f_{elec} as follows:

$$f_{\text{elec}} = -\mathbf{P}\cdot\mathbf{E} - \frac{1}{2}\mathbf{E}:\varepsilon_{\text{b}}:\mathbf{E}. \tag{5}$$

With cubic symmetry in the background material, there exists equivalent constant along three axes in the background dielectric tensor ε_{b}, i.e. $\varepsilon_{\text{b}} = \varepsilon_{11\text{b}} = \varepsilon_{22\text{b}} = \varepsilon_{33\text{b}}$.

Additionally, the surface energy is responsible for the relaxation of the polarization near the surfaces. Using the concept of extrapolation length, we write f_{surf} in tensor form as:

$$f_{\text{surf}} = \frac{1}{2}\mathbf{P}\cdot\boldsymbol{\omega}\cdot\mathbf{P} \tag{6}$$

where $\boldsymbol{\omega}$ denotes the surface coefficient as a second-order tensor, which is related to the extrapolation length δ_i^{eff}. For simplicity, we have neglected the influence of the asymmetry of the surfaces, or, we should alternatively add a first-order term [40]. Here, we adopt $\boldsymbol{\omega} = \text{diag}(D_1^{\text{s}}/\delta_1^{\text{eff}}, D_2^{\text{s}}/\delta_2^{\text{eff}}, D_3^{\text{s}}/\delta_3^{\text{eff}})$, with D_i^{s} the coefficient correlated to surface normal vector and gradient energy tensor [36].

The temporal evolution of the non-conservative polarization field of a ferroelectric can be captured via a phenomenological evolution equation, that is, the time-dependent Ginzburg–Landau (TDGL) equation:

$$\frac{\partial\mathbf{P}\left(\mathbf{r},t\right)}{\partial t} = -L\frac{\delta F}{\delta\mathbf{P}\left(\mathbf{r},t\right)} \tag{7}$$

where the kinetic coefficient L is related to the mobility of domain wall. The boundary conditions of the polarization can be obtained by letting the thermodynamic force to be zero, i.e. $\delta F/\delta\mathbf{P} = 0$,

$$\left(\mathbf{g}:\nabla\mathbf{P}\right)\cdot\mathbf{n} + \boldsymbol{\omega}\cdot\mathbf{P} = \mathbf{0} \tag{8}$$

where $\mathbf{n}$ denotes the surface normal vector.

Assume that the steady state of the electric field and mechanical stress/strain field can be achieved instantaneously as soon as the polarization field changes. Under such an 'adiabatic' treatment, we can calculate the electric field and mechanical stress/strain field according to the equilibrium equations. The mechanical equilibrium equations are as follows:

$$\nabla\cdot\boldsymbol{\sigma} = \mathbf{0} \tag{9}$$

where $\boldsymbol{\sigma} = \mathbf{C}:\mathbf{e}$ indicates stress tensor. For the ferroelectric nanodisk, the mechanical boundary conditions on the top and bottom surfaces are given by

$$\boldsymbol{\sigma}\cdot\mathbf{n}|_{\text{S}} = \boldsymbol{\tau}|_{\text{S}} \tag{10}$$

where $\boldsymbol{\tau}$ is the external stress vector.

We adopt the electrostatic equilibrium equation in the following form:

$$\nabla\cdot\mathbf{D} = 0 \tag{11}$$

where $\mathbf{D}$ is the electric displacement and can be expressed as

$$\mathbf{D} = \varepsilon_0\mathbf{E} + \boldsymbol{\chi}_{\mathbf{b}}\cdot\mathbf{E} + \mathbf{P} = \boldsymbol{\varepsilon}_{\mathbf{b}}\cdot\mathbf{E} + \mathbf{P} \tag{12}$$

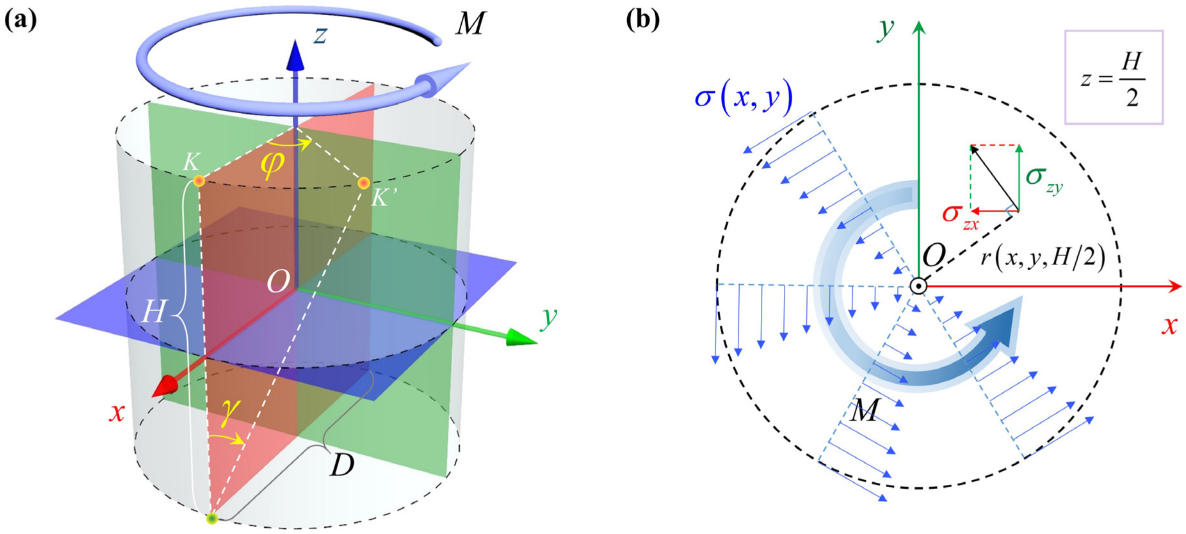

Figure 2. Schematics of the mechanical model of a nanodisk under torsion. (a) The 3D view of the mechanial model. (b) Stress distribution at the top surface of the nanodisk.

where ε_0 is the vacuum dielectric constant, and $\chi_\mathbf{b}$ is the background permittivity. Moreover, we consider open-circuit boundary condition at all the surfaces in this work as follows:

$$\mathbf{D}\cdot\mathbf{n}=0. \tag{13}$$

Note that here we assume that there are no free charges inside and at the surface of the system, as in equations (11) and (13), to mimic a poor screening condition so that the vortex state in ferroelectric nanodisks is favored.

2.2. Mechanical model

When a straight bar is subjected to a torsion stimuli, the exact solution of the torsional problem for a circular shaft is applicable if we assume that the cross-sections of the bar remain plane and rotate without any distortion during twist. This theory, developed by Coulomb, was applied later by Navier to bars of noncircular cross-sections. We employ this theory for investigations because it is appropriate to circular nanodisk in our work [48].

As depicted in figure 2(a), the Cartesian coordinates are attached to the nanodisk with the reference plane lying in the middle cross-section of the nanodisk and the origin of coordinates located in the center. The x, and y-axes lie in the reference plane, and the z-axis is the longitudinal axis perpendicular to the reference plane, as shown in figure 2(a). The in-plane coordinates of plane $z=H/2$ in the top view is shown in figure 2(b). Generally speaking, a positive torsion M satisfies the right-hand rule in the outer normal direction to the top and bottom surfaces of the nanodisk. In this work, we introduce an in-plane twist angle φ to mimic the effect of a torsion M applied to the nanodisk. Specifically, φ describes the torsional deformation of plane $z=H/2$ relative to the reference plane $z=-H/2$, and it is positive when measured counterclockwise (CCW) from the x-axis (see figure 2(b)).

According to the elementary theory of circular shafts, the shear stress distribution at any sections perpendicular to z axis is independent. Because the cross-section of the circular nanodisk is constant and the shear modulus is independent of position in the sample, the shear stress $\sigma(x, y)$ is homotopic in the axial direction. Moreover, the shear stress $\sigma(x, y)$ at any point of the cross-section is along the angle direction, and satisfies the generalized Hook's law, i.e. $\sigma=G\gamma$, where G is the shear modulus of material, and γ is the shear strain, standing for an axial twist angle between the plane $z=H/2$ and $z=-H/2$. In figure 2(a), under small deformation hypothesis, the point K is moved to point K' after the application of the torque M to the nanodisk. Obviously, due to the arc length of $\widehat{KK'}$, the twist angle φ and shear strain γ satisfy the relationship $\varphi D=2\gamma H$, where H and D are thickness and diameter of the circular nanodisk, respectively. Particularly, in plane $z=H/2$, resolving the shear stress into two components parallel to the x and y-axes, we find $\sigma_{zx}=-G\gamma x/r$ and $\sigma_{zy}=G\gamma y/r$, as shown in figure 2(b). Thus, we obtain $2\varepsilon_{zx}=-x\varphi/H$ and $2\varepsilon_{zy}=y\varphi/H$ in plane $z=H/2$. In addition, the torque M is derived by integration of shear stress on the plane, i.e. $M=\iint_\mathrm{S}(\sigma_{zx}\varepsilon_{zx}+\sigma_{zy}\varepsilon_{zy})\,\mathrm{d}S$. As a result, we find the proportional relationship between M and φ, i.e. $M=GJ\varphi/H$, where J is the polar moment of inertia of the circular cross-section. Therefore, for a given torque, the twist angle of the bar is inversely proportional to the centroidal polar moment of inertia J of the circular cross-section, and that the maximum shearing stress occurs at the most outside points from the center axis. In this work, considering the proportional relationship between M and φ, we use φ instead of M to denote the torsion applied to the PTO nanodisk in our simulations [45].

3. Numerical implementation

Here, we employ PTO nanodisks with circular and uniform cross-sections as the model systems. However, the conclusions of this work are not limited to nanodisk structure and PTO. Indeed, we found that conclusions of this work are also applicable to $BaTiO_3$ nanodisks in spite of structural phase transitions that can be involved during the state evolution at low temperature. Similar behaviors should appear in other nanostructures in materials with electrostrictive or magnetostrictive effects. The default dimensions are $D = 8\,\text{nm}$ and $H = 4\,\text{nm}$, otherwise they would be claimed explicitly. We adopt a grid of triangular prism element to discretize the system, in which the typical size of element is about 0.4 nm. The default temperature in the simulations is taken to be 300 K, otherwise it would be claimed explicitly. In this work, all the values of the parameters can be found in[4]. Particularly, the coefficients of Landau energy and elastic energy are taken from [41], the gradient energy coefficients are from [35], the coefficients of surface energy are from [42], and the background dielectric constant in electrostatic energy is from [33] and [34]. To characterize the vortex state of the nanodisk, we calculate the toroidization $\mathbf{G} = V^{-1}\int_V \mathbf{r} \times \left(\mathbf{P} - \overline{\mathbf{P}}\right)\mathrm{d}V$, where $\mathbf{r}$ stands for position vector, and $\overline{\mathbf{P}}$ for average polarization vector of system [43]. Moreover, to identify the chirality of the vortex states more clearly during the vortex transformation, the curl of the polarization field is also calculated, that is, $\mathbf{R} = \nabla \times \mathbf{P}$ [44]. The Euler iterative method is used to solve the TDGL equation (equation (8)) under the boundary conditions (equation (9)). The time step is chosen to be $\Delta t = 0.01 a_0 L$, where $a_0 = |a_1|_{T=300\,\text{K}}$. The simulation time of each field application stage is taken to be long enough so that the dipole state of the nanodisk is sufficiently relaxed into a steady state under the given field application. The electrostatic equilibrium equation (equation (12)) and the mechanical equation (equation (10)) are solved by finite element method (FEM) at each time step during the iteration of the TDGL equation (equation (8)).

4. Results and discussion

There are four main topics in the following analysis. Firstly, we investigate the effect of the torsion force on the stability of the vortex state in the PTO nanodisks. A Bloch-type quasi-skyrmion (BQS) state is found. Secondly, we reveal the topological feature of the BQS state and offer an explanation on the origin this state. The Pontryagin density and the topological charge of the BQS state are calculated, and the topological charge as a function of torsion and temperature is acquired. Thirdly, we elucidate the feasibility of mechanical and electrical switching of vortex in the ferroelectric nanodisks, basing on the trilinear coupling between the toroidization, polarization and shear strain of the system. Finally, several influential factors are considered to further reveal the regularity of vortex switching, including the temperature, torsion, electric field, and diameter of the nanodisk.

The processes of torsion-induced skyrmion-like state and torsion-induced vortex switching are schematically illustrated in figure 1. Here, as an example, we denote the CCW vortex state as the initial state ‘0’ and the clockwise (CW) vortex state as the final state ‘1’. With a CCW torsion ‘$+M$’ applied to the nanodisk, the initial vortex state ‘0’ will transform into a BQS state. Then, keeping the CCW torsion fixed, an external electric field along $+z$-axis ‘$+E$’ is applied and a stable helical state will be developed. Moreover, two types of vortex switching, namely, mechanical switching (Class-I) and electrical switching (Class-II) can be realized. For Class-I switching, if we apply a fixed external electric field along z-axis to the nanodisk, the two vortex states ‘0’ and ‘1’ can be switched to each other by reversing the torsion force. For Class-II switching, if we apply a fixed torsion force to the nanodisk, the two vortex states ‘0’ and ‘1’ can be switched to each other by reversing the external electric field along z-axis.

4.1. Effect of torsion on the vortex state

Now we investigate the influence of torsion and electric field on the vortex state in PTO nanodisks at room temperature. The diameter and height of the nanodisk is 8 nm and 4 nm, respectively. Four cases of vortex state evolution in the nanodisk with the combined application of the torsion and electric field are simulated. They are: (i) the evolution of vortex state ‘0’ under a CCW torsion (denoted as ‘$+M$ loading’) and afterwards under an external electric field along $+z$-axis with the CCW torsion fixed (denoted as ‘$+M$ fixed, $+E$ loading’); (ii) the evolution of vortex state ‘1’ under a CCW torsion (denoted as ‘$+M$ loading’) and afterwards under an external electric field along $-z$-axis with the CCW torsion fixed (denoted as ‘$+M$ fixed, $-E$ loading’); (iii) the evolution of vortex state ‘0’ under a CW torsion (denoted as ‘$-M$ loading’) and afterwards under an external electric field along $-z$-axis with the CW torsion fixed (denoted as ‘$-M$ fixed, $-E$ loading’); and (iv) the evolution of vortex state ‘1’ under a CW torsion (denoted as ‘$-M$ loading’) and afterwards under an external electric field along $+z$-axis with the CCW torsion fixed (denoted as ‘$-M$ fixed, $+E$ loading’). The stable dipole states at different loading conditions, and the evolution curves of the z-component of toroidization G_z and polarization P_z are shown in figure 3, with 3(a)–(d) corresponding to the four cases. Note, here we label the four degenerate states (i.e. the BQS states) as state S in the PTO nanodisk subjected to a torsion, and label the four degenerate states as A, B, C, and D in the PTO nanodisk subjected to a combination of torsion and electric field.

In figure 3(a), we choose the vortex state ‘0’ as the initial state. Note that the vortex state emerges as a ground state of the nanodisks due to the strong depolarization effect, similar to those formed in low dimensional ferroelectric nanostructures. After applying CCW torsion $+M$ (corresponding to $\varphi = 0.04$ rad) to the nanodisk, a distorted vortex state S is achieved. Such a state possesses an induced negative polarity. The polarization at the center of the nanodisk is along the $-z$-axis, but the polarization gradually changes to positive along the radial direction. The z-component of polarization distributed on the lateral side of the cylindrical nanodisk is 0.22 C m^{-2}, and that in the central region is -0.24 C m^{-2}. Note that this state is quite similar to the skyrmion state that is well

---

[4] $a_1 = 3.85\,(T - 752) \times 10^5$, $a_{11} = 7.3 \times 10^7$, $a_{12} = 7.5 \times 10^8$, $a_{111} = 2.6 \times 10^8$, $a_{112} = 6.1 \times 10^8$,$a_{123} = 3.7 \times 10^9$,$C_{11} = 1.746 \times 10^{11}$,$C_{12} = 0.7937 \times 10^{11}$, $C_{44} = 1.1111 \times 10^{11}$, $Q_{11} = 0.089$, $Q_{12} = -0.026$, $Q_{44} = 0.0675$, $G_{11} = 3.46 \times 10^{-10}$, $G_{12} = 0$, $G_{44} = 1.73 \times 10^{-10}$, $G_{14} = 1.73 \times 10^{-10}$, $G_{14} = G_{12} + G_{44}$, $D_i^{\mathrm{s}} = 3.46 \times 10^{-10}$, $\delta_i^{\mathrm{eff}} = 5 \times 10^{-9}$, $\varepsilon_{\mathrm{b}} = 4.425 \times 10^{-10}$ (in SI units).

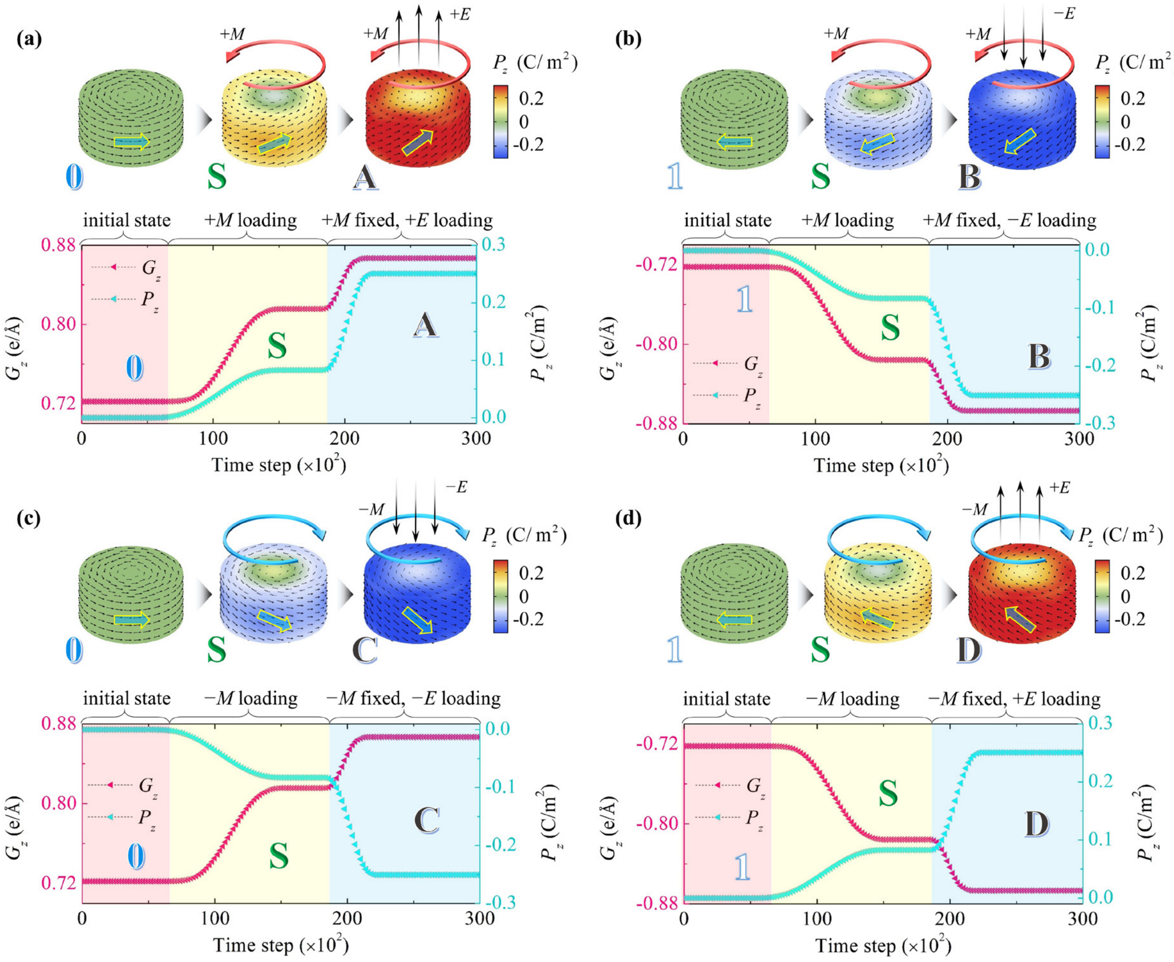

Figure 3. Vortex state evolution in the nanodisk under different combined applications of the torsion and electric field. (a) Evolution of vortex state '0' under a CCW torsion ('$+M$ loading') and afterwards under an external electric field along $+z$-axis with the CCW torsion fixed ('$+M$ fixed, $+E$ loading'). (b) Evolution of vortex state '1' under a CCW torsion ('$+M$ loading') and afterwards under an external electric field along $-z$-axis with the CCW torsion fixed ('$+M$ fixed, $-E$ loading'). (c) Evolution of vortex state '0' under a CW torsion ('$-M$ loading') and afterwards under an external electric field along $-z$-axis with the CW torsion fixed ('$-M$ fixed, $-E$ loading'). (d) Evolution of vortex state '1' under a CW torsion ('$-M$ loading') and afterwards under an external electric field along $+z$-axis with the CCW torsion fixed ('$-M$ fixed, $+E$ loading').

observed in ferromagnetic materials [47]. As we know, the topological charge Q is the most representative index for characterization of a skyrmion topological structure, and the Q of a skyrmion state is equal to $+1$ or -1. However, for state S, its topological charge is found to be smaller than 1 (its topological feature will be discussed in details in the next section). In fact, it is not a normal skyrmion but skyrmion-like because the outermost dipoles are not completely reversed compared with the central ones. That is why we call it as BQS state. Nevertheless, the discovery of such a state indicates that mechanical strain may be exploited to help stabilization of normal skyrmion states in ferroelectric materials. Starting with state S, we further apply an electric field '$+E$' (in magnitude of 4 MV cm^{-1}) to the nanodisk along $+z$-axis while keeping the torsion '$+M$' fixed. With the application of a torsion and the electric field, we obtain a new stable state denoted as A. We can see the disappearance of the downward polarization in the central region; in other words, the polarity changes from negative to positive due to the poling effect of the external electric field. The magnitude of polarization in the nanodisk becomes larger, and the orientation of polarization is more along the z direction than along the in-plane direction. In state A, the z-component of polarization distributed in the outermost region is 0.25 C m^{-2}, and that in the central region is 0.1 C m^{-2}. From the evolution curves of the z-component of toroidization G_z and polarization P_z (figure 3(a)), one can also see that the initial vortex state '0' has a G_z of 0.72 e Å^{-1} and a zero P_z. After the loading of a CCW torsion '$+M$', the nanodisk evolved into state S, which has a G_z of 0.82 e Å^{-1} and a P_z of 0.08 C m^{-2}. When an external electric field along $+z$-axis is applied with the CCW torsion fixed, the nanodisk finally adopts state A with G_z of 0.865 e Å^{-1}, and P_z of 0.25 C m^{-2}.

The second case of vortex state evolution in the nanodisk are similar to the first case. In figure 3(b), the initial vortex state is '1'. After applying a CCW torsion '$+M$', corresponding to $\varphi = 0.04$ rad, a BQS state S is also obtained, in which the z-component of polarization is positive at the center and gradually becomes negative along the radial direction from the inner to outer region of the cross-section in nanodisks. When the torsion '$+M$' is fixed, the application of an

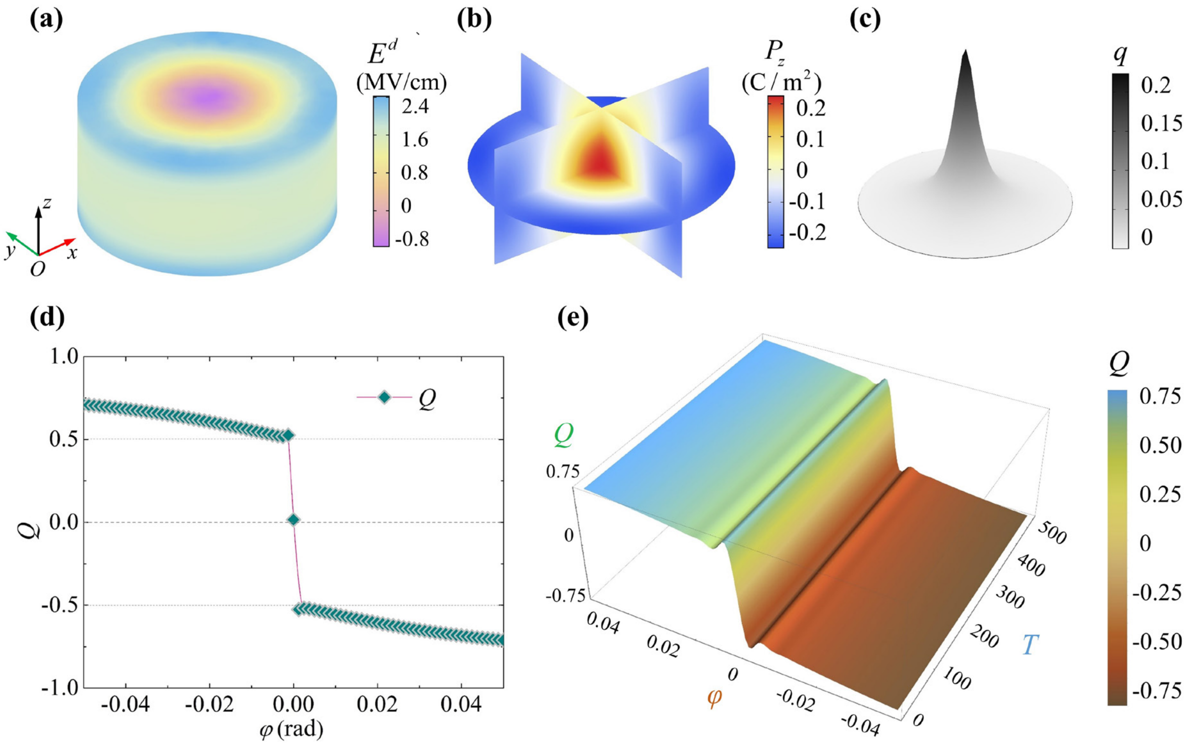

Figure 4. The origin and topological characterization of the BQS state found in figure 3(b). (a) The depolarization field E^d along z-axis of the BQS state. (b) 3d plots of P_z in the BQS state. (c) The Pontryagin density q of the BQS state at the cross-section $z = 0$. (d) The topological charge Q of the BQS state as a function of the twist angle φ at the cross-section $z = 0$. (e) The dependence of Q on temperature and φ.

electric field $E = -4$ MV cm^{-1} can result in a stable state B, in which the dipoles rotate in the in-plane direction to form a CW vortex and orient along the $-z$-axis to form an out-of-plane polar order. Such an evolution of the vortex state is also reflected in the corresponding evolution curves of toroidization G_z and polarization P_z. Moreover, from the evolution curves shown in figures 3(a) and (b), one can notice that G_z and P_z show a positive correlation (i.e. have the same sign) when applying CCW torsion to the PTO nanodisk.

The effect of CW torsion on the vortex state evolution in the nanodisk is depicted in figures 3(c) and (d), corresponding to the third and fourth cases, respectively. As shown in figure 3(c), we start from the initial vortex state '0'. Similar to the previous two cases, after applying a CW torsion '$-$ M' (corresponding to $\varphi = -0.04$ rad), a BQS state S is obtained, in which the z-component of polarization is positive in the central region and gradually becomes negative along the radial direction. With the torsion '$-$ M' being fixed, the application of an electric field $E = -4$ MV cm^{-1} can result in a stable state C, in which all the dipoles are distributed to form an in-plane CCW vortex and an out-of-plane polar order. For the initial vortex state '1' (figure 3(d)), after applying a CW torsion '$-$ M' (corresponding to $\varphi = -0.04$ rad), it also evolves into a BQS state S, in which the z-component of polarization is negative in the central region and gradually becomes positive along the radial direction. With the torsion '$-$ M' being fixed, the application of an electric field $E = +4$ MV cm^{-1} results in a stable state D, which has both an in-plane vortex and a polar order along z-axis. From the evolution curves of in figures 3(c) and (d), one can see that G_z and P_z of the vortex states show a negative correlation (i.e. have different signs) during the application of CW torsion to the PTO nanodisk. This is in contrast with the previous cases with CCW torsion application.

Unlike in ferromagnetic materials, there is usually only chirality but no polarity of the vortex in ferroelectrics. However, the polarity of vortex state in PTO nanodisk can be induced by torsion, and BQS states can be thus developed. With an external torsion applied to the nanodisk, due to the electrostrictive effect, geometric deformation of the nanodisk induced by torsion causes the dipoles to reorient from lying in-plane to tilting to the out-of-plane direction. Thus, the polarity of vortex can be induced and controlled by an external torsion. Moreover, by manipulation of external stimuli including torsion and electric field, the transformation between four basic degenerate stable states A, B, C and D may inspire us to propose new strategies of vortex switching.

4.2. Topological feature of the BQS state

In this section, we would like to further discuss the origin of the BQS state and reveal its topological feature. The BQS state S of case (ii) in figure 3(b) is taken for discussion. The depolarization field E^d along z-axis of the S state is depicted in figure 4(a). As mentioned above, the dipoles at the central region of the nanodisk are oriented opposite to those close to the outer region. This phenomenon is believed to be caused by the depolarization effect. While the torsion tends to induce a tilting of the dipole toward to the z-axis, the dipoles are not likely to all orient along the same out-of-plane direction, as the depolarization field will be too high to keep the state stable. In order to lower the electrostatic energy, the dipoles tend to form configurations with smaller depolarization field such as 180° domain structure or vortex state. In this case, a vortex order already exists in the in-plane direction, and the dipoles near the vortex core are most vulnerable to rotate due to their small magnitudes. Under the influence of the local depolarization field, the dipoles near core reverse to $+z$ direction. As a result, we find a BQS state S in PTO nanodisks after the application of a torsion. From the 3D plots of P_z as depicted in figure 4(b), we can see that after forming the BQS state, the core can maintain a quite large P_z of about $+0.22$ C m^{-2}, which is comparable to that in the outmost region -0.24 C m^{-2}.

In order to quantify the topological nature of the BQS state, the Pontryagin density q of the BQS state S is depicted in figure 4(c). The Pontryagin density q is expressed as the following definition, i.e. $q = \frac{1}{4\pi}\mathbf{p}\cdot\left(\frac{\partial \mathbf{p}}{\partial x}\times\frac{\partial \mathbf{p}}{\partial y}\right)$, where the three-component vector $\mathbf{p}$ denotes the normalized local dipole moment [46, 49, 50]. For a skyrmion, the topological charge Q can be calculated via the surface integral of the Pontryagin density in (0 0 1) plane, i.e. $Q = \int q\mathrm{d}x\mathrm{d}y$. As we know, in ferromagnetic systems, the topological charge Q is ± 0.5 for a vortex, and $Q = \pm 1$ for a skyrmion [47], whereas in ferroelectric systems, Q is zero for a normal ferroelectric vortex due to the absence of core polarity. In recent years, skyrmion bubbles have been theoretically predicted in BaTiO$_3$/SrTiO$_3$ nanocomposites [46] and PbTiO$_3$/SrTiO$_3$ superlattices [51]. However, neither of these predictions are in single-phase ferroelectrics. In this work, with the introduction of torsion, one can obtain a skyrmion-like state in single-phase ferroelectrics. As we mentioned above, the BQS state is actually an incomplete Bloch-type skyrmion because the outermost dipoles is not completely reversed to the central ones. This can be also seen from the value of the topological charge. In figure 4(d), we calculate the relation between topological charge Q and the twist angle φ. It shows that Q is about 0.74 for $\varphi = 0.05$ rad, which is smaller than 1. With the increase of $|\varphi|$, Q can be more closer to 1. When $\varphi > 0$ (i.e. CCW torsion '$+M$'), we get $Q < 0$, with a negative polarity at the core. When $\varphi = 0$ (zero torsion), we have $Q = 0$, corresponding a normal ferroelectric vortex state. When $\varphi < 0$ (CW torsion '$-M$'), we get $Q > 0$, with a positive polarity at the core. Furthermore, the dependence of Q on temperature and φ is depicted in figure 4(e). One can see that the topological charge of the torsion-induced skyrmion-like state is insensitive to the temperature.

4.3. Effect of torsion on the chirality of the vortex: Class-I switching

In this and the next sections, we investigate the feasibility of vortex switching in PTO nanodisks by applying torsion and electric field. Torsion plays a significant role in the stabilization of distorted states with polarity (i.e. the BQS state, A, B, C, and D states) in the nanodisks. The four degenerate states A, B, C, and D as shown in figure 3 actually suggest the feasibility of vortex switching. One can carry out appropriate manipulation to realize the control of vortex chirality by mutual transformation between state A and D (C) and (B), or A and B (C) and (D). Note, we have investigated the shear contribution for polarization switching from the viewpoint of energy previously [31]. According to the Landau–Ginzburg–Devonshire (LGD) theory, utilizing the contribution of the shear part in the electrostrictive effect, a portion of the elastic energy density, which is expressed as $f' = \frac{1}{2}(\sigma_{xz}\varepsilon^0_{xz} + \sigma_{yz}\varepsilon^0_{yz}) = \frac{1}{2}Q_{44}P_z(\sigma_{xz}, \sigma_{yz})\cdot(P_x, P_y)$, also implies that the chirality of in-plane vortex state can be tuned by the multiple external stimulus to satisfy the principle of energy minimization. In fact, we can see the trilinear relationship among P_z, $(\sigma_{xz}, \sigma_{yz})$, and (P_x, P_y). In order to satisfy $f' < 0$, if we fix the orientation of P_z while change the orientation of $(\sigma_{xz}, \sigma_{yz})$, we can reverse the orientation of (P_x, P_y), i.e. G_z. Similarly, if we fix the orientation of $(\sigma_{xz}, \sigma_{yz})$ while change the orientation of P_z, we can also reverse G_z. Therefore, based on this electromechanical coupling relation, two types of manipulation for vortex switching can be proposed: One is fixing the electric field while reversing the torsion, defined as Class-I switching, which corresponds to the processes A $\rightleftharpoons$ D (C $\rightleftharpoons$ B); the other one is fixing the torsion while reversing the axial electric field, defined as Class-II switching, which corresponds to the processes A $\rightleftharpoons$ B (C $\rightleftharpoons$ D).

Here, we conduct a simulation of Class-I switching for the process A $\rightarrow$ D. As shown in figure 5(a), snapshots of the vortex evolution of the nanodisk are depicted. Here, the curl of polarization $\mathbf{R}$, is employed as the reference index to characterize the vortex chirality. The color shown in the domain patterns in figure 5(a) is defined by R_z, which is equal to $(\partial P_y/\partial x - \partial P_x/\partial y)$. As the magnitude of R_z at the vortex core in '0' and '1' state is opposite in sign, one can clearly see the changes in the vortex chirality during the switching process. We define E_f as the fixed electric field and choose state '0' as the initial vortex state. The evolution curves of G_z and P_z of the nanodisk are presented in figure 5(b). In the initial state '0', G_z and P_z of the nanodisk are 0.72 e Å^{-1} and 0 C m^{-2}, respectively. As the time step reaches 6000, an axial electric field '$+E$' (corresponding to $E_\mathrm{f} = 4$ MV cm^{-1}) and a CCW torsion '$+M$' (corresponding to $\varphi = 0.04$ rad) are applied to the nanodisk. We find that the nanodisk evolves into state A with G_z and P_z being 0.865 e Å^{-1} and 0.25 C m^{-2}, respectively. After that, the electric field '$+E$' is kept fixed. As the time step reaches 18 000, a CW torsion '$-M$' ($\varphi = -0.04$ rad) is applied to the nanodisk. Then we find that the nanodisk evolves into state D with G_z and P_z being -0.865 e Å^{-1} and 0.25 C m^{-2}, respectively. Finally, after unloading both the torsion and electric field, the nanodisk relaxes to state '1', in which G_z and P_z are -0.72 e Å^{-1} and 0 C m^{-2}, respectively. As a result, the vortex chirality of the nanodisk is reversed via Class-I switching.

In mechanics, for an isotropic material that obeys Hooke's law, a shear strain is defined as a change in angle between the same line before and after deformation. The distributions

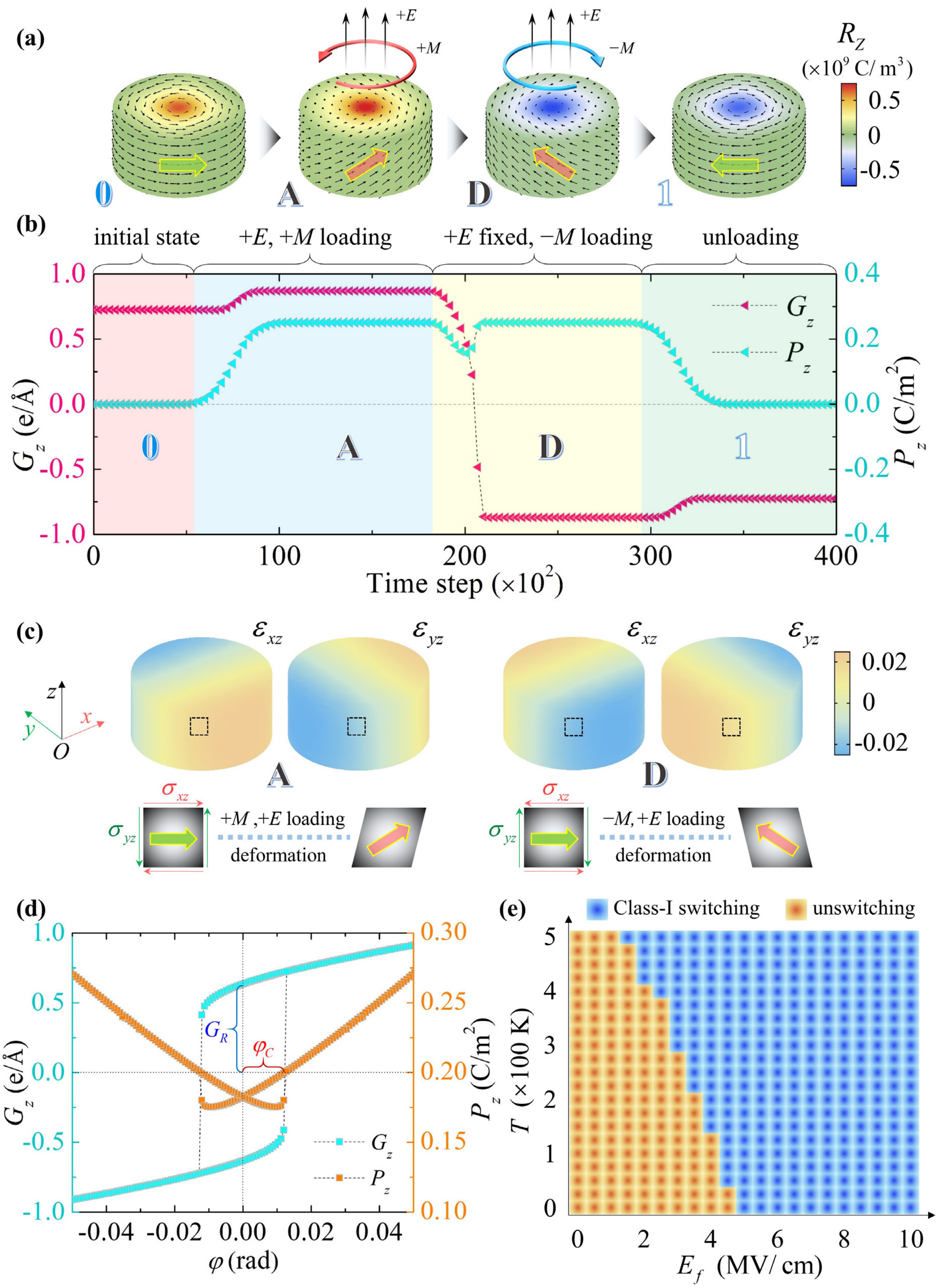

Figure 5. Simulation results of Class-I switching. (a) Evolution snapshots of the vortex state and (b) evolution curves of G_z and P_z during the switching process. (c) The distributions of ε_{xz} and ε_{yz} in states A and D. (d) The hysteresis loops of G_z and P_z in response to the twist angle φ under the condition of a fixed electric field $E_f = 4$ MV cm^{-1} at room temperature. (e) Switching phase diagram as a function of temperature and the fixed electric field E_f.

of ε_{xz} and ε_{yz} in states A and D are depicted in figure 5(c). A tiny element right in front of the nanodisk is selected for analysis of shear deformation in response to torsion loading. Obviously, ε_{xz} and ε_{yz} in the element are positive and negative in state A, respectively. The shear strain induced by torsion tends to cause the dipoles to tilt to the out-of-plane direction. Moreover, due to the effect of '$+E$', a $+z$-axial helix dipole configuration with a CCW vortex order on the cross-section is favored. Similarly, in state D, in response to the reversal of torsion, ε_{xz} and ε_{yz} in the element become negative and positive, respectively. As a result, the dipoles is redistributed into a new $+z$-axial helix with a CW vortex order in the xy plane.

Furthermore, we investigate the hysteresis loop between the twist angle φ and G_z and that between φ and P_z. The switching between state A and D is clearly indicated by these hysteresis loops, as shown in figure 5(d). In this simulation, the external electric field is fixed as $E_{\mathrm{f}} = +4$ MV cm^{-1} at all the time. The axial toroidization G_z is determined by the in-plane components of polarization P_x and P_y. As the electric field is fixed, the magnitudes of P_x and P_y are determined by M (corresponding to φ). In state A and D, with increasing $|\varphi|$, the magnitude of the dipoles becomes larger while the inclination angle of the dipoles to the xy plane decreases. Both changes increase the magnitudes of P_x and P_y, and $|G_z|$ increases consequently. $|G_z|$ and $|\varphi|$ thus exhibit a positive correlation with each other. As shown in figure 5(d), the shape of the hysteresis loop between G_z and φ looks like a parallelogram, whereas the one between P_z and φ is in butterfly shape. The coercive twist angle φ_{C} is 0.013, and the remanent toroidization G_{R} is 0.64 e Å^{-1}. Moreover, a switching phase diagram as a function of temperature and the fixed electric field E_{f} is shown in figure 5(e). A border between Class-I switching and unswitching regions is clearly seen. With increasing the temperature, Class-I switching becomes more feasible and the minimum value of E_{f} decreases in an almost linear trend (with a slope of about -0.6 MV cm^{-1} per 100 K). Also via Class-I switching, the processes C $\rightleftharpoons$ B are similar to the processes A $\rightleftharpoons$ D and are not shown here.

4.4. Effect of torsion on the chirality of vortex: Class-II switching

In this section, we further discuss Class-II switching exemplified by the processes from A to B. The snapshots of vortex evolution of the nanodisk are depicted in figure 6(a). Here, we also employ the curl of polarization $\mathbf{R}$ as the reference index to characterize the vortex chirality. The color shown in the domain patterns in figure 6(a) is defined by R_z. We choose state '0' as the initial vortex state, and define φ_{f} as the fixed twist angle. The evolution curves of G_z and P_z of the nanodisk are presented in figure 6(b). In the initial vortex state '0', G_z and P_z of the nanodisk are 0.72 e Å^{-1} and 0 C m^{-2}, respectively. As the time step reaches 6000, a CCW torsion '$+M$' (corresponding to $\varphi_{\mathrm{f}} = 0.04$ rad) and an axial electric field '$+E$' (4 MV cm^{-1}) are applied to the nanodisk, we find that the nanodisk would evolve into state A with G_z and P_z being 0.865 e Å^{-1} and 0.25 C m^{-2}, respectively. After that, the torsion '$+M$' ($\varphi_{\mathrm{f}} = 0.04$ rad) is kept fixed. As the time step reaches 18 000, an axial electric field '$-E$' (-4 MV cm^{-1}) is applied to the nanodisk. Then we find that the nanodisk evolves into state B with G_z and P_z being -0.865 e Å^{-1} and -0.25 C m^{-2}, respectively. Note that if the applied time of the electric field is not enough to switch the vortex state, the vortex state will reduce to the initial vortex state after loading, and would not display an intermediate state after loading under the current circumstance. Finally, after unloading both the torsion and the electric field, the vortex relaxes to state '1', in which G_z and P_z are -0.72 e Å^{-1} and 0 C m^{-2}, respectively. Class-II switching is completed.

Similar to the previous section, the distributions of ε_{xz} and ε_{yz} in state A and B are shown in figure 6(c) to help understand the switching mechanism. A tiny element right in front of the nanodisk is selected for analysis of shear deformation in response to torsion loading. Due to the same torsion loading '$+M$' to the nanodisk, the stress and strain states in A and B are identical. As shown in figure 6(c), for both state A and B, ε_{xz} and ε_{yz} in the element are positive and negative, respectively. Moreover, due to the effect of '$+E$', a $+z$-axial helix dipole configuration with a CCW vortex order in the xy plane is favored (state A). In contrast, due to the reversed external electric field, the dipoles form a $-z$-axial helix configuration, exhibiting a CW vortex order in the xy plane, is developed in state B.

Furthermore, we investigate the hysteresis loops between E and G_z as well as the loop between E and P_z. From these hysteresis loops, one can clearly see the switching between state A and B, as shown in figure 6(d). In this simulation, a CCW torsion '$+M$' (corresponding to $\varphi_{\mathrm{f}} = 0.04$ rad) is kept fixed at all times. Unlike those in figure 5(d), the shapes of the two loops in figure 6(d) both look like a parallelogram. In particular, it should be noted that the hysteresis loop between G_z and E is somewhat different from a traditional one. When the torsion '$+M$' is fixed, the magnitudes of the polarization components P_x and P_y are determined by E. In state A and B, with an increasing $|E|$, the magnitude of the dipoles becomes larger meanwhile the inclination angle of the dipoles to the xy plane increases. The former change tends to increase $|G_z|$, whereas the latter tends to reduce it. The competition of these two effects induces a gradual bending of the hysteresis loop between G_z and E. In fact, if $|E|$ continues to increase to a sufficiently large value, $|G_z|$ will approach zero. As shown in figure 6(d), the coercive electric field E_{C} is 3.0 MV cm^{-1}, and the remanent toroidization G_{R} is 0.82 e Å^{-1}. A switching phase diagram as a function of temperature and the fixed twist angle φ_{f} is exhibited in figure 6(e). It can be seen that, with increasing the temperature, the minimum value of φ_{f} of Class-II switching decreases rapidly in a nonlinear way. Also via Class-II switching, the processes C $\rightleftharpoons$ D are similar to the processes A $\rightleftharpoons$ B and are not shown here.

4.5. Effects of various factors on vortex switching

To further reveal the regularity of vortex switching in nanodisk via the manipulation of torsion and electric field, we consider the effects of some factors on the feasibility of vortex switching in the section. These factors include: temperature

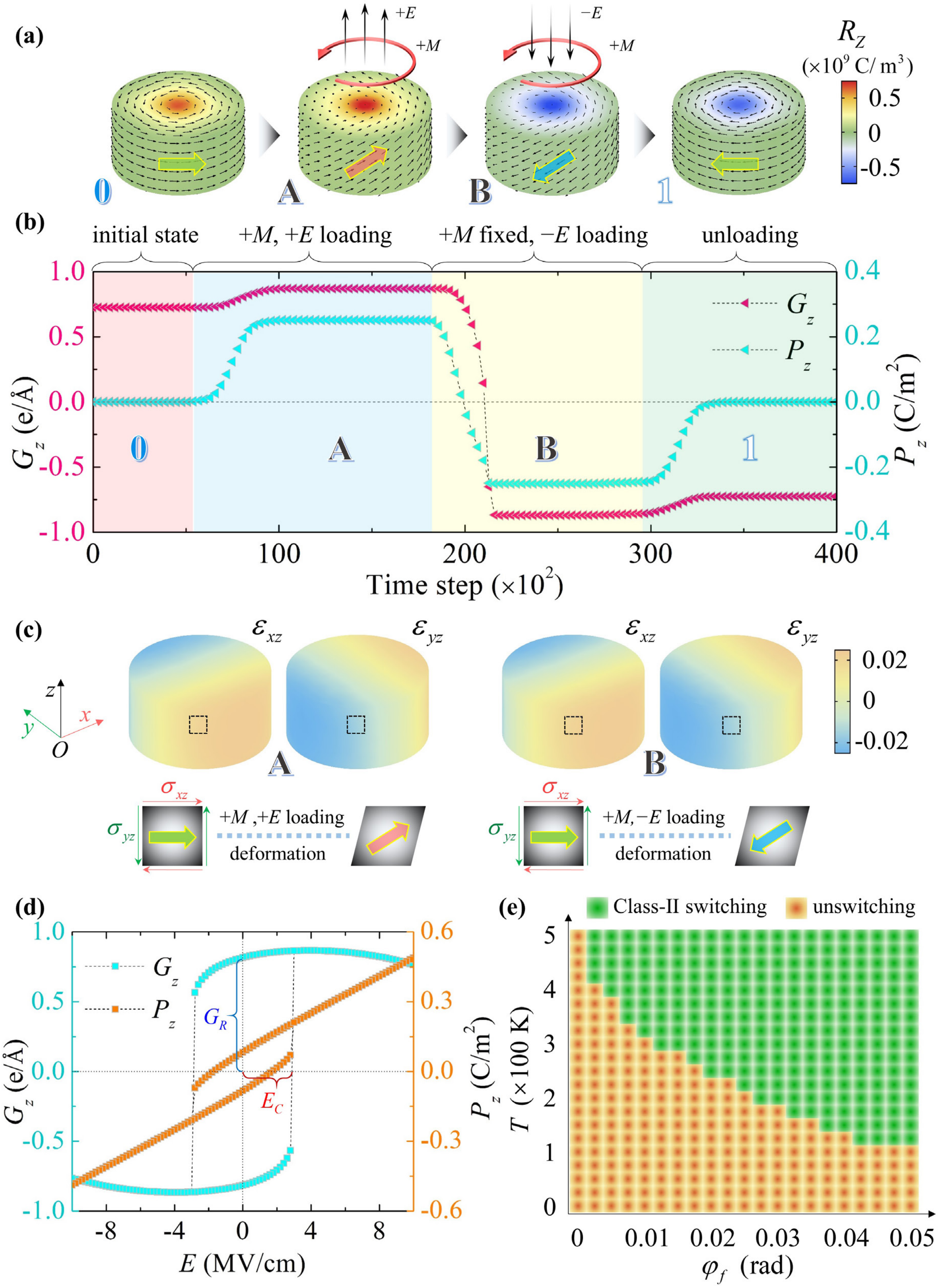

Figure 6. Simulation results of Class-II switching. (a) Evolution snapshots of the vortex state and (b) evolution curves of G_z and P_z during the switching process. (c) The distributions of ε_{xz} and ε_{yz} in states A and B. (d) The hysteresis loops of G_z and P_z in response to the electric field E under the condition of a fixed twist angle $\varphi_\mathrm{f} = 0.04$ rad at room temperature. (e) Switching phase diagram as a function of temperature and the fixed twist angle φ_f.

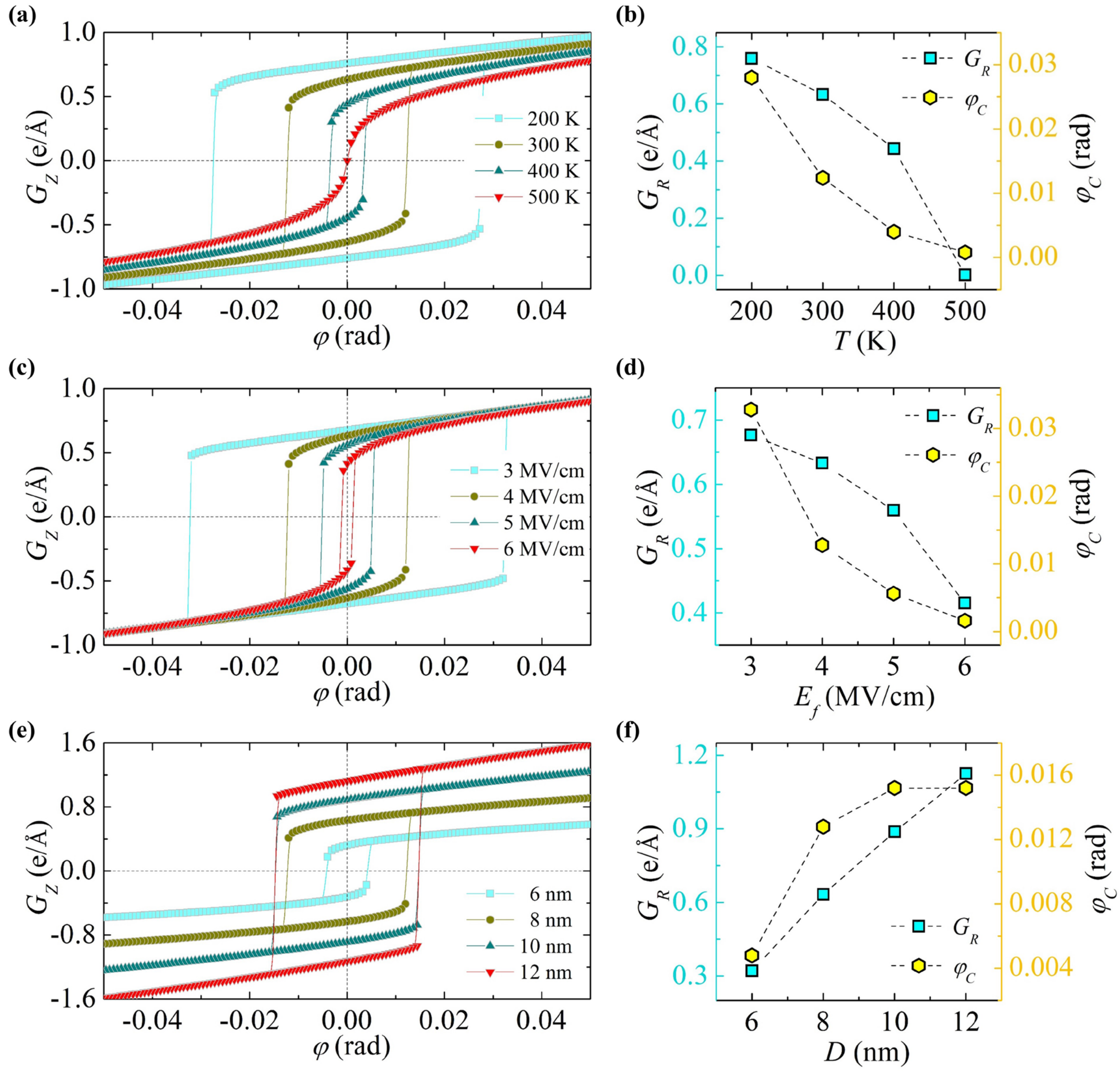

Figure 7. Influence of various factors on Class-I switching. (a) The hysteresis loops between G_z and φ at different temperatures. (b) The dependence of G_R and φ_C on temperature. (c) The hysteresis loops between G_z and φ under different fixed electric fields. (d) The dependence of G_R and φ_C on the fixed electric field. (e) The hysteresis loops between G_z and φ in nanodisks with different diameters. (f) The dependence of G_R and φ_C on the nanodisk diameter.

T, the fixed loadings (i.e. E_f for Class-I switching and φ_f for Class-II switching) and the nanodisk diameter D. We depict hysteresis loops between G_z and the control variables (i.e. φ for Class-I switching and E for Class-II switching) under the different conditions, and analyze the changes of the remanent G_R and coercive values of the control variables (denoted as φ_C for Class-I switching and E_C for Class-II switching). If not mentioned, here we adopt the following default settings: $T = 300\,\text{K}$, $D = 8\,\text{nm}$, $E_f = 4$ MV cm^{-1}, and $\varphi_f = 0.04$ rad.

We investigate the effect of temperature (T), fixed electric field (E_f), and nanodisk diameter (D) on control of the vortex chirality by Class-I switching, and the results are presented in figure 7. Firstly, the effect of temperature is considered in our simulations. The simulation temperatures range from 200 K to 500 K. The hysteresis loops between G_z and φ are shown in figure 7(a). With an increasing T, the hysteresis loops exhibit a sharp shrinkage. This indicates that it is easier to control the chirality of vortex by Class-I switching at a higher temperature. At $T = 200\,\text{K}$, the coercive twist angle φ_C is 0.028 rad, and the remanent toroidization G_R is 0.76 e Å^{-1}. At $T = 400\,\text{K}$, φ_C and G_R decrease to be 0.012 rad and 0.45 e Å^{-1}, respectively. However, the hysteresis disappears when T increases to 500 K. In fact, G_R and φ_C are both equal to 0 at $T = 500\,\text{K}$, which implies that a pure polar state is formed in PTO nanodisks due to the poling effect of the fixed electric field ($E_f = 4$ MV cm^{-1}). For this case, the application of torsion can induce the vortex order, with its chirality determined by the sign of the torsion. However, such an induced vortex order cannot maintain stable after unloading the torsion. In figure 7(b), we display the dependence of G_R and φ_C on temperature. It is clear that G_R and φ_C are negatively correlated with temperature.

The effect of fixed electric field E_f on the control of the vortex chirality by Class-I switching is shown in figures 7(c) and (d), where a series of hysteresis loops between G_z and φ,

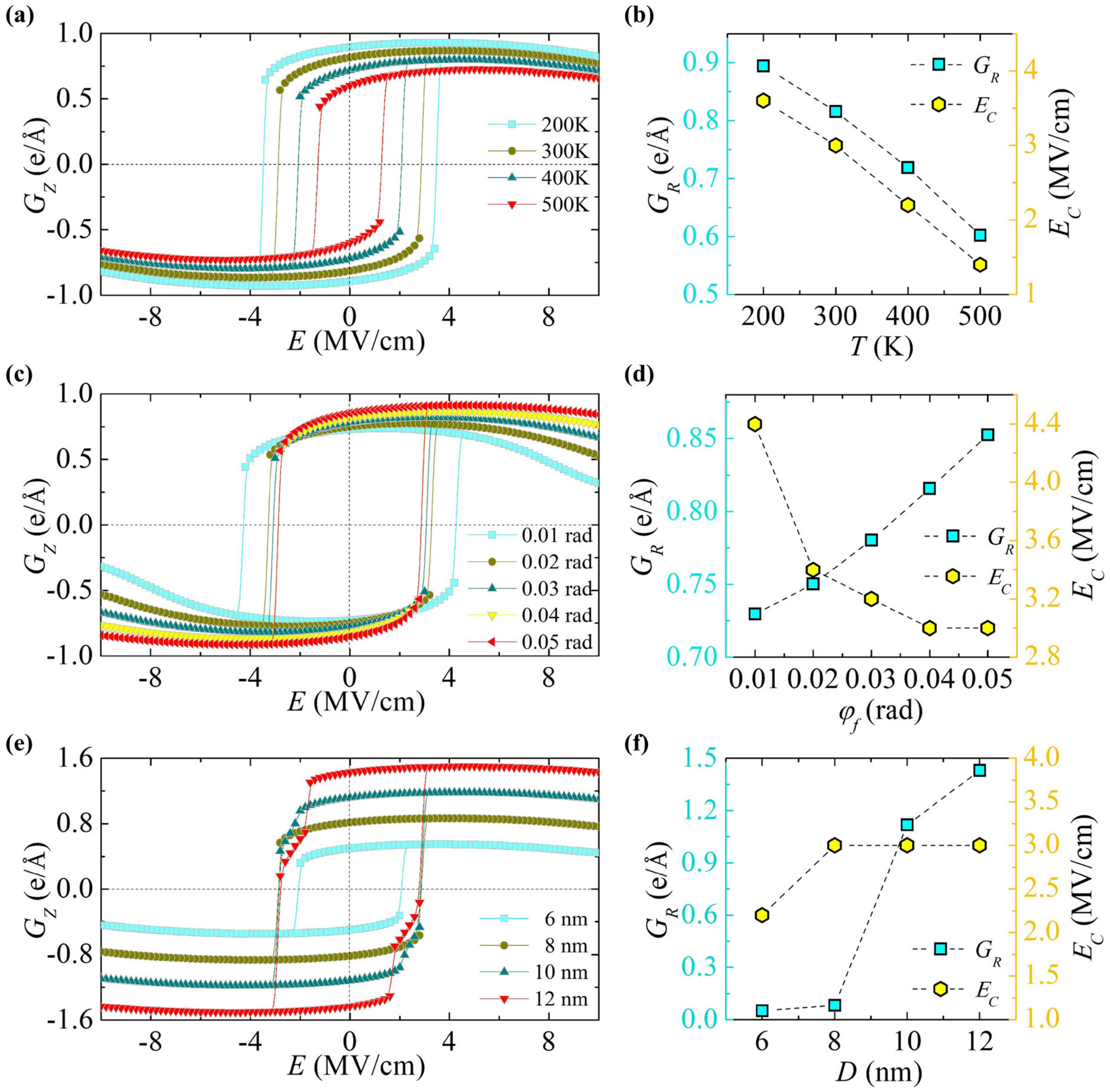

Figure 8. Influence of various factors on Class-II switching. (a) The hysteresis loops between G_z and E at different temperatures. (b) The dependence of G_R and E_C on temperature. (c) The hysteresis loops between G_z and E under different fixed twist angles. (d) The dependence of G_R and E_C on the fixed twist angle. (e) The hysteresis loops between G_z and E in nanodisks with different diameters. (f) The dependence of G_R and E_C on the nanodisk diameter.

and the curves of G_R and φ_C as functions of E_f are depicted, with E_f ranging from 3 MV cm^{-1} to 6 MV cm^{-1}. When E_f equals to 3 MV cm^{-1}, i.e, when it takes the smallest value, the hysteresis loop is the largest, with φ_C and G_R being 0.034 rad and 0.675 e Å^{-1}, respectively. With the increase of E_f, the hysteresis loop becomes narrower, and φ_C and G_R rapidly decrease. As E_f reaches 6 MV cm^{-1}, the hysteresis loop becomes quite narrow, with φ_C and G_R being 0.002 rad and 0.42 e Å^{-1}, respectively. The negative correlation of G_R and φ_C with E_f is easy to be understood considering the fact that the axial electric field enhances the polar order and depress the vortex order, which leads to a decrease of toroidization and a lower energy barrier between the two vortex states with opposite chirality.

The effect of cross-sectional diameter D of nanodisk on vortex switching by Class-I switching is shown in figures 7(e) and (f). The diameters range from 6 nm to 12 nm. The hysteresis loops between G_z and φ are exhibited in figure 7(e). The dependence of G_R and φ_C on the cross-sectional diameter D of the nanodisk is depicted in figure 7(f). For a larger D, the hysteresis loop is larger. The results indicate that it is easier to control the chirality of the vortex by Class-I switching for a smaller nanodisk. At $D = 6$ nm, the coercive twist angle φ_C is 0.004 rad, and the remanent toroidization G_R is 0.38 e Å^{-1}. At At $D = 12$ nm, φ_C and G_R increase to 0.016 rad and 1.15 e Å^{-1}, respectively. One can see that both of φ_C and G_R have positive correlations with D. This reflects the fact that, the larger size of nanodisk, the more stable of the vortex order.

Afterwards, as depicted in figure 8, we investigate the effect of temperature (T), fixed torsion (φ_f), and nanodisk diameter (D) on the control of vortex chirality by Class-II switching, respectively. Firstly, different temperatures ranging from 200 K to 500 K are considered. The hysteresis loops between G_z and E are shown in figure 8(a). Similar to the case of Class-II switching, with an increasing T, the hysteresis loops exhibit a sharp shrinkage, indicating that there are more difficulties in reversing the chirality of the vortex by Class-I switching at a lower temperature. At $T = 200\,\text{K}$, the coercive electric field E_C is 3.6 MV cm^{-1}, and the remanent toroidization G_R is 0.896 e Å^{-1}. At $T = 500\,\text{K}$, E_C and G_R decrease to 1.4 MV cm^{-1} and 0.602 e Å^{-1}, respectively. The dependence of G_R and E_C on temperature is shown in figure 8(b). We can see that both G_R and E_C are negatively correlated with temperature, reflecting the fact that at lower temperature, the vortex order is more stable and the energy barrier of vortex switching is larger.

The effect of fixed twist angles φ_f on the control of the vortex chirality is shown in figures 8(c) and (d). In figure 8(c), a series of hysteresis loops between G_z and E are depicted with φ_f ranging from 0.01 rad to 0.05 rad. It is worth noting the minor differences in the shapes of various hysteresis loops. When φ_f is at a minimum, i.e. equal to 0.01 rad, the remanent toroidization G_R is also at a minimum of 0.726 e Å^{-1}. However, the coercive electric field E_C is the largest and equal to 4.4 MV cm^{-1} at $\varphi_\text{f} = 0.01$ rad. In an extreme case, if the external fixed torsion is zero (corresponding to $\varphi_\text{f} = 0$), it is impossible to reverse the chirality of the vortex alone by applying an external z-axial electric field E, regardless of how large it is. Thus we can see that G_R has a positive correlation with φ_f, in contrast with the case of E_C. This is also clearly seen in figure 8(d), where the curves of G_R and E_C as functions of φ_f are plotted. The opposite dependence of G_R and E_C on φ_f is due to that φ_f enhances the stability of the vortex order while it depresses the axial polar order.

Finally, vortex switching in nanodisks with different diameters D ranging from 6 nm to 12 nm are simulated. The hysteresis loops between G_z and E are shown in figure 8(e). In figure 8(f), we also depict the curves of G_R and E_C as functions of D. One can see that with the increasing of D, the hysteresis loops become larger. At $D = 6\,\text{nm}$, the coercive electric field E_C is 2.2 MV cm^{-1} and the remanent toroidization G_R is 0.05 e Å^{-1}. At $D = 12\,\text{nm}$, E_C and G_R increase to be 3.0 MV cm^{-1} and 1.42 e Å^{-1}, respectively. This result indicates that the vortex state in smaller nanodisks is easier to be switched. This is similar to the previous result of Class-I switching. In general, both φ_C (for Class-I switching) and E_C (for Class-II switching) are positively correlated with D, a result due to the fact that the larger size of nanodisk the more stable of the vortex order. It is noteworthy that the hysteresis curve deviates from a parallelogram when the diameter increases. This is due to the appearance of an intermediate state at low field regime, where a CW (CCW) vortex is nested in a larger CCW (CW) vortex.

Note, the effects of the nanodisk height on the BQS state and vortex switching are not shown in this work. Our further results show that the height effects are stronger at small height regime due to the stronger depolarization effect at this regime, leading to smaller polarization and toroidization. Nevertheless, in general, the effects of the nanodisk height on the BQS state and vortex switching are small, compared to those of nanodisk diameter, due to the fact the toroidal order is in the transverse (xy) plane. Even for nanodisk in 2 nm height, its BQS state and vortex switching curves are still almost the same with those of larger heights.

5. Summary and discussion

In summary, we have investigated the effect of torsion on the controllability of vortex state in ferroelectric nanodisks. A novel type of skyrmion-like state (named BQS state) is identified. The origin and topological feature of the BQS state are explored. Moreover, we propose two strategies for the deterministic control of vortex chirality, named Class-I switching and Class-II switching. For Class-I switching, if we apply a fixed external electric field along z-axis to the nanodisk, the two degenerated vortex states '0' and '1' can be switched to each other by reversing the torsion force. For Class-II switching, if we apply a fixed torsion force to the nanodisk, the two vortex states can be switched to each other by reversing the external electric field along z-axis. We further reveal the influences of temperature, electric field, torsion, and diameter of the nanodisk on the vortex switching. Phase diagrams of vortex switching are summarized. In general, our work elucidates the feasibility of vortex switching via electromechanical coupling, which should provide insights into the practical control and applications of ferroelectric vortex.

The discovery of a BQS state in nanodisk indicates that mechanical strain may be exploited to help stabilization of normal skyrmion states in ferroelectric materials. This is instructive for the search of strain-stabilized topological dipole states in single phase ferroelectric, and provides new ideas of developing multi-order functional devices for future applications. The new strategies of vortex switching takes advantage of the shear contribution of electrostrictive effect in ferroelectrics. This is different from the current mainstream mechanisms based on the symmetry breaking of the vortex nucleation and annihilation. It should be pointed out that the torsion loading is still challenging at the nanoscale operation in experiment. A type of press-induced twist-tip making use of 3D printing technique may solve this problem in future [52].

Acknowledgments

The authors acknowledge support from NSFC (Nos. 11672339, 11474363, 11572355, 11602310, 11232015). Yue Zheng also acknowledges the support from the Special Program for Applied Research on Super Computation of the NSFC Guangdong Joint Fund, the Fok Ying Tung Foundation, the Guangdong Natural Science Funds for Distinguished Young Scholar and the China Scholarship Council.

ORCID iDs

Weijin Chen https://orcid.org/0000-0002-9276-7369

References

[1] Landau L D and Lifshitz E M 1935 *Phys. Z. Sowjet.* **8** 153
[2] Kittel C 1946 *Phys. Rev.* **70** 965
[3] Naumov I I, Bellaiche L and Fu H 2004 *Nature* **432** 737
[4] Gruverman A, Wu D, Fan H J, Vrejoiu I, Alexe M, Harrison R J and Scott J F 2008 *J. Phys.: Condens. Matter* **20** 342201
[5] Rodriguez B J, Gao X S, Liu L F, Lee W, Naumov I I, Bratkovsky A M, Hesse D and Alexe M 2009 *Nano Lett.* **9** 1127
[6] Jia C L, Urban K W, Alexe M, Hesse D and Vrejoiu I 2011 *Science* **331** 1420
[7] Nelson C T *et al* 2011 *Nano Lett.* **11** 828
[8] McGilly L J and Gregg J M 2011 *Nano Lett.* **11** 4490
[9] Stachiotti M G and Sepliarsky M 2011 *Phys. Rev. Lett.* **106** 1
[10] Balke N *et al* 2011 *Nat. Phys.* **8** 81
[11] Tang Y L *et al* 2015 *Science* **348** 547
[12] Yadav A K *et al* 2016 *Nature* **530** 198
[13] Hong Z J Q *et al* 2017 *Nano Lett.* **17** 2246
[14] Damodaran A R *et al* 2017 *Nat. Mater.* **16** 1003
[15] Li Z *et al* 2017 *Sci. Adv.* **3** e1700919
[16] Morozovska A N, Eliseev E A and Glinchuk M D 2007 *Physica* B **387** 358
[17] Tagantsev A K, Cross L E and Fousek J 2010 *Domains in Ferroic Crystalls and Thin Films* (Berlin: Springer)
[18] Wang B and Woo C H 2005 *J. Appl. Phys.* **97** 84109
[19] Gregg J M 2012 *Ferroelectrics* **433** 74
[20] Prosandeev S, Ponomareva I, Kornev I, Naumov I and Bellaiche L 2006 *Phys. Rev. Lett.* **96** 237601
[21] Naumov I and Fu H 2007 *Phys. Rev. Lett.* **98** 077603
[22] Naumov I and Fu H 2008 *Phys. Rev. Lett.* **101** 197601
[23] Chen W J, Zheng Y and Wang B 2012 *Sci. Rep.* **2** 796
[24] Chen W J, Zheng Y and Wang B 2012 *Appl. Phys. Lett.* **100** 062901
[25] Fu X, Naumov I I and Fu H 2013 *Nano. Lett.* **13** 491
[26] Chen W J, Zheng Y and Wang B 2015 *Sci. Rep.* **5** 11165
[27] Dubovik V M and Tugushev V V 1990 *Phys. Rep.* **187** 145
[28] Prosandeev S, Ponomareva I, Kornev I and Bellaiche L 2008 *Phys. Rev. Lett.* **100** 047201
[29] Chen W J and Zheng Y 2015 *Acta Mater.* **88** 41
[30] Yuan S, Chen W J, Ma L L, Ji Y, Xiong W M, Liu J Y, Liu Y L, Wang B and Zheng Y 2018 *Acta Mater.* **148** 330
[31] Chen W J, Yuan S, Ma L L, Ji Y, Wang B and Zheng Y 2018 *RSC Adv.* **8** 4434
[32] Tagantsev A K 2008 *Ferroelectrics* **375** 19
[33] Zheng Y and Woo C H 2009 *Appl. Phys.* A **97** 617
[34] Woo C H and Zheng Y 2008 *Appl. Phys.* A **91** 59
[35] Wang J J, Ma X Q, Li Q, Britson J and Chen L Q 2013 *Acta Mater.* **61** 7591
[36] Chen W J, Zheng Y, Wang B, Ma D C and Ling F R 2013 *Phys. Chem. Chem. Phys.* **15** 7277
[37] Hlinka J and Marton P 2006 *Phys. Rev.* B **74** 104104
[38] Khachaturyan A G 1983 *Theory of Structure Transformations in Solids* (New York: Wiley)
[39] Landau L D, Lifshitz E M and Pitaevskii L P 1984 *Electrodynamics of Continuous Media* (Oxford: Oxford University Press)
[40] Tagantsev A K, Gerra G and Setter N 2008 *Phys. Rev.* B **77** 174111
[41] Pertsev N A, Zembilgotov A G and Tagantsev A K 1998 *Phys. Rev. Lett.* **80** 1988
[42] Ishikawa K and Uemori T 1999 *Phys. Rev.* B **60** 11841
[43] Zheng Y and Chen W J 2017 *Rep. Prog. Phys.* **80** 86501
[44] Li Q, Nelson C T, Hsu S L, Damodaran A R, Li L L, Yadav A K, McCarter M, Martin L W, Ramesh R and Kalinin S V 2017 *Nat. Commun.* **8** 1468
[45] Wang J, Li G P, Shimada T, Fang H and Kitamura T 2013 *Appl. Phys. Lett.* **103** 242413
[46] Nahas Y, Prokhorenko S, Louis L, Gui Z, Kornev I and Bellaiche L 2015 *Nat. Commun.* **6** 8542
[47] Fert A, Reyren N and Cros V 2017 *Nat. Rev. Mater.* **2** 17031
[48] Timoshenko S P and Gere J M 1985 *Theory of Elastic Stability* (New York: McGraw-Hill)
[49] Nagaosa N and Tokura Y 2013 *Nat. Nanotechnol.* **8** 899
[50] Zhou Y and Ezawa M 2014 *Nat. Commun.* **5** 4652
[51] Hong Z and Chen L Q 2017 *Acta Mater.* **152** 155
[52] Frenzel T, Kadic M and Wegener M 2017 *Science* **358** 1072